JGR Space Physics

RESEARCH ARTICLE
10.1029/2022JA030460

Plasmoids in the Jovian Magnetotail: Statistical Survey of Ion Acceleration Using Juno Observations

A. Blöcker[1], E. A. Kronberg[1], E. E. Grigorenko[2], G. Clark[3], L. Kozak[4], M. F. Vogt[5], and E. Roussos[6]

[1]Department of Earth and Environmental Sciences, Ludwig-Maximilians-University, Munich, Germany, [2]Space Research Institute, Russian Academy of Sciences, Moscow, Russia, [3]Johns Hopkins University Applied Physics Laboratory, Laurel, MD, USA, [4]Astronomy and Space Physics Department, Kyev Taras Shevchenko University, Kyev, Ukraine, [5]Center for Space Physics, Boston University, Boston, MA, USA, [6]Max Planck Institute for Solar System Research, Göttingen, Germany

Key Points:

- Intensity of heavy ions is strongly increased during plasmoids close to the current sheet center
- Significant increase of heavy ion intensities is observed in plasmoids with larger wave power
- Acceleration of heavy and light ions in plasmoids due to resonant interaction with the magnetic field fluctuations could not be observed

Correspondence to:
A. Blöcker,
a.bloecker@lmu.de

Citation:
Blöcker, A., Kronberg, E. A., Grigorenko, E. E., Clark, G., Kozak, L., Vogt, M. F., & Roussos, E. (2022). Plasmoids in the Jovian magnetotail: Statistical survey of ion acceleration using Juno observations. *Journal of Geophysical Research: Space Physics*, *127*, e2022JA030460. https://doi.org/10.1029/2022JA030460

Received 15 MAR 2022
Accepted 31 JUL 2022

Abstract Transient magnetic reconnection plays an important role in energetic particle acceleration in planetary magnetospheres. Jupiter's magnetosphere provides a unique natural laboratory to study processes of energy transport and transformation. Strong electric fields in spatially confined structures such as plasmoids can be responsible for ion acceleration to high energies. In this study we focus on the effectiveness of ion energization and acceleration in plasmoids. Therefore, we present a statistical study of plasmoid structures in the predawn magnetotail, which were identified in the magnetometer data of the Juno spacecraft from 2016 to 2018. We additionally use the energetic particle observations from the Jupiter Energetic Particle Detector Instrument which discriminates between different ion species. We are particularly interested in the analysis of the acceleration and energization of oxygen, sulfur, helium, and hydrogen ions. We investigate how the event properties, such as the radial distance and the local time of the observed plasmoids in the magnetotail, affect the ion intensities close to the current sheet center. Furthermore, we analyze if ion acceleration is influenced by magnetic field turbulence inside the plasmoids. We find significant heavy ion acceleration in plasmoids close to the current sheet center which is in line with the previous statistical results based on Galileo observations conducted by Kronberg et al. (2019, https://doi.org/10.1029/2019JA026553). The observed effectiveness of the acceleration is dependent on the position of Juno in the magnetotail during the plasmoid event observation. Our results show no correlation between magnetic field turbulence and nonadiabatic acceleration for heavy ions during plasmoids.

1. Introduction

The understanding of the mechanisms which are responsible for strong ion acceleration in the magnetotail is not only an important topic of interest in the Earth's magnetosphere but also in other planetary magnetospheres, such as Jupiter's magnetosphere. The dynamics in Earth's and Jupiter's magnetospheres show similarities and differences. At Earth, the solar wind forms the major plasma source in the magnetosphere and is the main driver of the magnetospheric dynamics. Magnetic substorms are the consequence of transient global reconfigurations of the magnetic field topology. During the substorms energy is rapidly released to the magnetotail. However, at Jupiter the dynamics are more likely rotationally driven due to the unique properties of Jupiter's magnetosphere (Vasyliunas, 1983). Jupiter's magnetosphere constitutes the largest magnetosphere in our solar system with a fast spin period and the volcanically active moon Io as the primary magnetospheric plasma source. The interaction between Io's SO_2 atmosphere and the Jovian magnetospheric plasma leads to a mass loss from Io in form of ions and neutrals of about 1 ton per second (e.g., Thomas et al., 2004). The SO_2 dissociates into S and O. In the inner-to-middle magnetosphere ($\leq$40 R_J) the origin of the heavy ions is thought to be iogenic with predominantly O^+ and S^{++} and with a small contribution of O^{++}, S^+, and S^{+++} (e.g., Clark et al., 2020; Kim et al., 2020). Carbon at about 4.5–18.4 MeV/nuc from the solar wind was also detected in the middle magnetosphere (Cohen et al., 2001). In the outer magnetosphere light ions, H^+ and He^{++}, which originate from the solar wind become more abundant (e.g., Haggerty et al., 2009). Due to interchange motion, this plasma is transported from the source region outward by centrifugally driven mass-loaded flux tubes (Khurana et al., 2004, and references therein). The flux tubes stretch radially out down tail on the nightside via centrifugal force and eventually break off. The resulting reconnection process releases plasmoids from the plasma sheet propagating tailward. The mechanism how thermal ions can get accelerated to the superthermal energies in the magnetotail plasma sheet is very poorly understood. Both adiabatic and nonadiabatic processes are responsible for the ion acceleration in the magnetotail.

Plasmoids are often described as plasma bubbles on closed magnetic field loops of disconnected field lines or on helical magnetic fields called flux ropes (see e.g., Slavin et al., 1989). Reconnection processes and the associated ejection of plasmoids from the magnetotail were observed at Earth (e.g., Angelopoulos et al., 2008), Jupiter (e.g., Vogt et al., 2010), Saturn (e.g., Jackman et al., 2014), Mercury (e.g., Slavin et al., 2012), Mars (Eastwood et al., 2012), and Uranus (DiBraccio & Gershman, 2019). The perturbations of the radial magnetic field and the meridional magnetic field component are used as key parameters for identifying magnetospheric processes, such as magnetic reconnections, dipolarizations, and plasmoids. A bipolar signature in the meridional magnetic field component is associated with the spacecraft encountering a magnetic reconnection site or a plasmoid from a reconnection site (e.g., Slavin et al., 2003).

Global reconfiguration of the magnetic field topology at Jupiter's magnetotail was detected in the magnetic field and energetic particle data of the Galileo spacecraft and studied by, for example, Kronberg et al. (2005; 2008), Vogt et al. (2010; 2014), Woch et al. (1999). Nonadiabatic acceleration of ions during reconfiguration events in Jupiter's magnetotail was investigated by Kasahara et al. (2011), Kronberg et al. (2012; 2019), Radioti et al. (2007). Radioti et al. (2007) focused on the ion composition in the substorm-like events in the predawn region in the Jovian magnetotail and proposed small-scale magnetic field variations as a possible mechanism for particle energization. In the process they saw that sulfur and oxygen ions were more effectively energized than helium ions and protons. Kronberg et al. (2012) investigated acceleration of particles which is associated with the formation of a magnetic X-line. Kasahara et al. (2011) examined particle acceleration associated with dipolarization fronts in the Jovian tail. Using measurements from Galileo's magnetometer and multispecies ion observations of hydrogen, oxygen and sulfur from the Energetic Particle Detector (EPD) in the energy range from 22 to 1250 keV/nuc, Kronberg et al. (2019) investigated the transfer of the electromagnetic energy to the particle energy. From a statistical study of 14 plasmoids detected in the Jovian magnetotail, they showed that sulfur and oxygen ions are accelerated effectively by plasmoids and that electromagnetic turbulence in plasmoids plays an essential role in their acceleration. With the statistical study, they showed that the energy spectral indices of oxygen and sulfur ions at energy ranges between 30 and 400 keV/nuc decrease with the wave power. This observed decrease was in agreement with their test particle simulation results. They concluded that energy is transferred in plasmoids from electromagnetic waves to oxygen and sulfur particles yielding an effective acceleration with a wave power threshold of the order of 10 nT^2/Hz which is similar to the threshold in terrestrial plasmoids (Grigorenko et al., 2015). Observations of hydrogen ions at 220–1250 keV/nuc did not reveal acceleration in the plasmoids implying that hydrogen ions are affected by processes other than wave-particle interaction and/or that the time and energy resolution of the observations was too coarse for the analysis of hydrogen ions. Because of the sparse Galileo observations, ion dynamics and ion acceleration mechanisms in the plasmoids in the Jovian magnetotail are still poorly understood and require further investigation.

Since July 2016 the Juno spacecraft provides rich data sets acquired in Jupiter's magnetosphere. Recently, Vogt et al. (2020) presented a survey of 232 tail reconnection signatures observed in magnetic field data collected by the Juno spacecraft during its first 16 orbits of Jupiter. Artemyev et al. (2020) investigated heavy ion acceleration by dipolarizations observed with Juno. The role of the Jovian plasmoids detected with Juno in the ion acceleration has not been studied yet. Therefore, in this study we investigate the plasmoids observed in the Jovian magnetotail, where especially strong ion acceleration is expected, and present statistics on the acceleration and energization of oxygen, sulfur, helium and hydrogen ions inside the plasmoids similar to the study of the plasmoids detected in Galileo data by Kronberg et al. (2019). For the detection of the plasmoids in the magnetic field data we focus on the bipolar events identified in the survey of Vogt et al. (2020). In Section 2 we describe the Juno data applied in this study, and in Section 3 we present the properties of the identified plasmoids such as their duration and distribution and compare the properties to those identified in the Galileo data. Then in Section 4 we describe the methodology and present one plasmoid event. In Section 5 we present the results from the statistical analysis of ion intensities, wave power, and energy spectral index in plasmoids and compare these results to those derived from the plasmoids identified in the Galileo data. We finish with a summary in Section 6.

2. Juno Data

In this study we focus on the measurements of Juno's 16 orbits taking place during July 2016 and October 2018. For each selected plasmoid event, we examine the observations from the magnetometer (MAG) (Connerney et al., 2017) and Juno Energetic particle Detector Instrument (JEDI) (Mauk et al., 2017) which are onboard

NASA's Juno spacecraft. MAG is a vector fluxgate magnetometer which measures the magnetic field components. For each magnetic field component we use the data with a time resolution of 1 s. JEDI provides electron, high- and low-energy ion fluxes, including species separation. The measured species are electrons and ions of H, He, O, and S. JEDI measures the energy and angular and compositional distributions for ions at 20–50 keV to more than 1 MeV. The instrument has three specific sensors (JEDI-90, JEDI-180, and JEDI-270), which differ in the angle they are mounted to the spacecraft deck with respect to the magnetometer. Each of the sensors has 6 look directions over a 160° viewing fan. JEDI-90 and JEDI-180 sensors observe within the spacecraft equatorial plane. The sensors use a time-of-flight (TOF) and solid-sate detector (SSD) energy system. A detailed description of all sensors is given in Mauk et al. (2017). We use data from the JEDI-90 sensor since this sensor data is available for all of the plasmoid events we analyze here. We take the average ion fluxes over all angular directions. Most of the ion measurements in this study were taken when JEDI was in a low-energy-resolution mode. The energy ranges of the ion fluxes are calculated from the average of the bounds of the energy passbands over the look directions in the low-energy-resolution mode. The oxygen ion fluxes are grouped to energy ranges of (382–597, 598–941, 942–1599 keV). The sulfur ion fluxes are grouped to energy ranges of (498–759, 760–1151, 1152–1858 keV). The helium ion fluxes are grouped to energy ranges of (60–133, 135–375, 376–1296 keV). The hydrogen ion fluxes are grouped to energy ranges of (44–73, 74–126, 127–277, 278–555, 557–1222 keV).

The data in this study is presented in the right-handed Jupiter System III coordinates. The z axis is defined by the spin axis of Jupiter. r is pointing away from Jupiter. The longitude ϕ is parallel to the jovigraphic equator and is measured from the positive x axis (prime meridian) in direction of the positive y axis. The colatitude θ completes the right-handed system and is positive southward.

3. Identification of Plasmoids Using MAG Data

For the identification of plasmoid (PM) structures we consider the list of reconnection events which were identified in the MAG data from Juno's first 16 orbits of Jupiter by an automated detection algorithm by Vogt et al. (2020). They found 232 reconnection events but they did not specifically identify plasmoid events. Their list contains the B_θ sign classification during each event which gives us the possibility to select the "B_θ bipolar" events. Plasmoids can be identified by a bipolar structure in the meridional component of the magnetic field. Following Vogt et al. (2010), an event is defined bipolar if B_θ remains negative for 15%–85% of the event duration. We examine the data of the days of the 79 bipolar events in the reconnection list of Vogt et al. (2020) and select events with a clear plasmoid structure in the B_θ component. Jupiter's background equatorial field is southward oriented so that the undisturbed B_θ is positive. For the identification of plasmoids we apply the following criteria: B_θ increases above the background value ($+|B_{\theta,\mathrm{bg}}|$) which is the 10-hr running average of $|B_\theta|$ (see Vogt et al., 2010). The increase is followed by a change of sign of B_θ with a negative value of B_θ which is larger than $-|B_{\theta,\mathrm{bg}}|$. Then we require that B_θ crosses through zero and becomes positive again. We assign the start of the plasmoid as the enhancement of B_θ over $|B_{\theta,\mathrm{bg}}|$ and the end of the plasmoid as the change of sign of B_θ from negative to positive values. Following Vogt et al. (2020), the change of the sign of B_θ could provide information whether the plasmoid was moving tailward (positive-to-negative change) or planetward (negative-to-positive change). Since the ion plasma moments are not available yet, we consider the change of the B_θ sign as a proxy for the flow direction and take only events with a positive-to-negative change of B_θ into account. This magnetic signature is expected during a tailward moving plasmoid. Plasmoid signatures which are immediately followed by another plasmoid signature are considered as one plasmoid signature in our analysis. From the identified plasmoid structures we choose the events which were close to the current sheet center during the plasmoid signature, that is, the radial magnetic field component is <2 nT at some point during the plasmoid. We select only the PM events for which the particle data is available and the plasmoid signature lasts longer than 5 min so that the duration is larger than the particles' typical gyroperiods. Furthermore, we choose plasmoids which were embedded in a quiet magnetic field environment during the observations, that is, the magnitude of the magnetic field did not show large scale fluctuations in the time interval before the start of the plasmoid signature. We use the standard deviation σ as a measure for the variability of $|B|$ in the 25 min time interval before the start of the PM signature and choose only PM events with $\sigma < 1$ nT for our analysis. With this limitation we try to avoid that other magnetospheric effects (such as dipolarization fronts shortly before the start of the PM) other than plasmoids affect the ion fluxes before and inside the PM. If more than one plasmoid event is identified during 1 day, we calculate the duration between the end of one PM signature and the start of the following PM signature so that only PM events

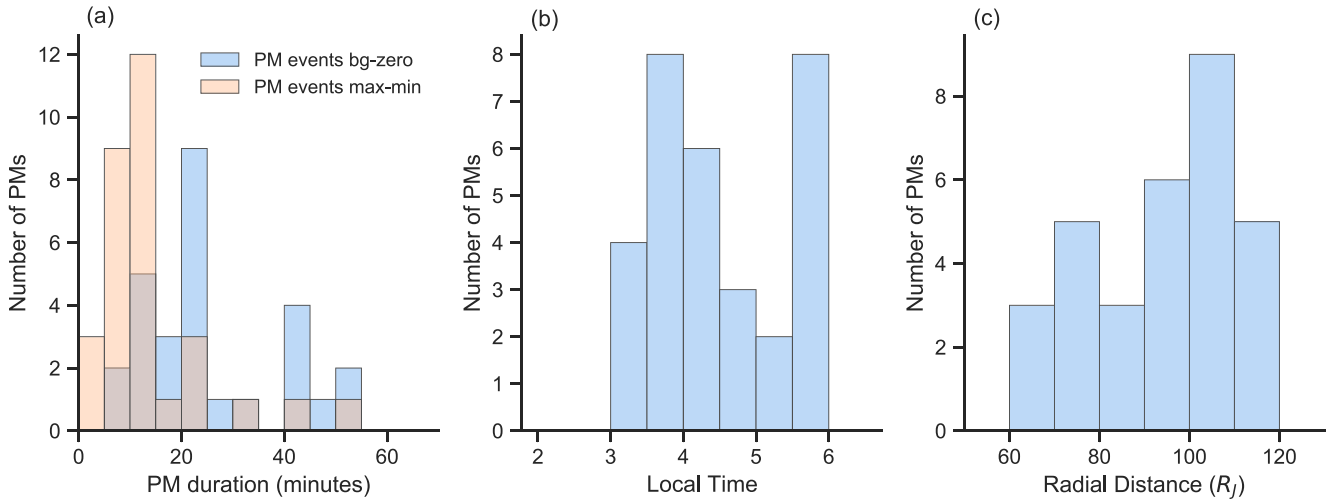

Figure 1. Histograms of different plasmoid properties for 31 plasmoid (PM) events used in this study: (a) Duration of the PMs as defined in the presented study with the start of the PM at the increase of B_θ from the background (bg) value and the end of the PM with the zero crossing of B_θ from negative to positive values (blue histogram) and the duration of the PMs as defined by Vogt et al. (2014) from the maximum to the minimum of B_θ (orange histogram). Three plasmoids with a duration of 90, 180, and 203 min are not shown in this histogram. (b) Number of PMs in dependence on the local time of the observations. (c) Number of PMs in dependence on the radial distance from Jupiter.

which are 25 min apart from each other are taken into account for the analysis in the time interval 25 min before the start of the PM signature.

3.1. Plasmoid Distribution and Properties

Figure 1 shows histograms of different properties of the PM events. We defined the duration of a PM as the time from the increase of B_θ over the background value ($|B_{\theta,\mathrm{bg}}|$) to the zero crossing from negative to positive values of B_θ. With this definition the average duration of the 31 PMs is 38 min and the median duration is 22 min. In Figure 1a we display a histogram of the duration for each plasmoid (blue histogram). It is visible that the analyzed plasmoids peak at a duration in the range between 20 and 25 min (9 PMs). Vogt et al. (2014) used another definition of the duration of a PM: The time between the maximum and minimum B_θ. With this definition of the duration most of the PMs in our study last between 5 and 15 min with an average duration of 14 min which is displayed in the orange histogram. Three PMs which lasted more than 80 min are not displayed in the blue histogram. Since such a long duration is not visible in the orange histogram, the long duration of these three PMs are due to a long lasting post plasmoid plasma sheet (PPPS) or due to two combined PM signatures. Vogt et al. (2014) derived a mean duration (from maximum to minimum B_θ) of about 7 min from 43 PMs observed by Galileo (see figure 7 in Vogt et al., 2014) which is in the range of the PM duration that we observe in the Juno data (orange histogram). Kronberg et al. (2019) analyzed 14 PM events of the 43 PMs identified in the Galileo data and calculated a median duration of about 36 min (see table 1 in Kronberg et al., 2019) using the same definition for the duration of a PM as we use in our study. In the Galileo data most of the PMs were detected at post-midnight local times between 01:30 and 03:00 LT (see figure 7 in Vogt et al., 2014). Juno's first 16 orbits have been confined to post-midnight/pre-dawn local times (02:00–06:00 LT). The comparison of the spatial coverage of Juno and Galileo orbits is shown in figure 2 in Vogt et al. (2020). Most of the PMs analyzed here were identified in the predawn local time sector between 03:30 LT and 04:30 LT and between 05:30 LT and 06:00 LT (see Figure 1b).

PMs observed with Galileo were mostly located between 80 and 110 R_J radial distance from Jupiter (see figure 7 in Vogt et al., 2014). In the Juno data, we see a peak of PM events at a similar location between 90 R_J and 110 R_J (see Figure 1c).

4. Methods

The purpose of our study is to investigate the effectiveness of ion acceleration in plasmoids in the Jovian magnetotail and how the acceleration is affected by the event properties. To do so, we analyze the relation between the ion intensity, wave power, energy spectral index and the distance from the current sheet center during the plasmoid events. In this section we explain the methods which we apply for the calculation of the wave power and the energy spectral index and present these methods for one PM event example.

4.1. Wavelet Transformation

For the analysis of the intensity of energetic ions and protons we apply a similar method as it was used in the study of plasmoids observed with Galileo by Kronberg et al. (2019). However, we conduct the wavelet analysis differently compared to Kronberg et al. (2019). We use a wavelet analysis with the Morlet wavelet (Torrence & Compo, 1998) to the azimuthal component of the magnetic field, B_ϕ, in order to calculate the frequency and wave power of the fluctuations. The wavelet analysis applied on the magnitude of the magnetic field, $|B|$, led to very similar results of the wave power in the statistical studies (shown in Section 5) as the wavelet analysis applied on B_ϕ. However, since we assume that the magnetic field fluctuations are related to Alfvénic fluctuations and we would like to exclude other signals related to for example, PMs, we chose B_ϕ for the wavelet analysis. Kronberg et al. (2019) applied the wavelet analysis to the meridional component of the magnetic field, B_θ, but B_θ fluctuations are contaminated by those associated with the plasmoid. For the calculation of the wave power we use the same assumptions as Kronberg et al. (2019): (a) The magnetic field fluctuations are related to the Alfvén waves and the plasmoid propagation velocity is nearly Alfvénic (Kronberg et al., 2008, 2019) with a bulk speed of 350–500 km/s (Kronberg et al., 2008). The magnetic field fluctuations are transported by the bulk flow tailward. Therefore, we have to take the Doppler effect into account and subtract the Doppler shift from the observed frequency range in the spacecraft frame. This leads to a shift of the frequencies to lower frequencies in the plasma rest frame. Following Grigorenko et al. (2015), the frequency f_0 in the plasma rest frame is given by $f_0 = f_{SC} - f_{SC}\frac{v}{v_{ph}}$, where f_{SC} is the observed frequency of the magnetic field fluctuations, v is the bulk velocity of the plasmoid, and v_{ph} is a wave phase velocity. Here it is assumed that the wave propagates in the same direction as the tailward moving plasmoid. $\frac{v}{v_{ph}}$ can be approximated by the Alfvén Mach number (see Kronberg et al., 2019). (b) The most probable range of the Alfvén Mach number lies between 0.6 and 0.9 (see Kronberg et al., 2008) and therefore the frequency range of interest for our analysis lies between $f_0 = (1 - 0.9)f_{SC} = 0.1f_{SC}$ and $f_0 = (1 - 0.6)$ $f_{SC} = 0.4f_{SC}$ (c) The ions interact most effectively with waves at the corresponding ion gyrofrequency (Grigorenko et al., 2015). Therefore, the wave frequency in the plasma rest frame f_0 should be equal to the gyrofrequency f_{gi} of the corresponding ion.

In order to calculate the integrated wavelet power from the spectrum of the magnetic field fluctuations in the spacecraft frame for the corresponding ion, the integration range of the ion gyrofrequencies in the spacecraft frame is shifted to the frequency range between $f_{gi} = 0.1f_{SC}$ and $f_{gi} = 0.4f_{SC}$. In this range the large variation of the possible plasmoid velocities relatively to the Alfvén velocity is taken into account. The frequency band for O^+ in one PM event is indicated by the black lines and the power is shown by the color scale in Figure 2b. At each time step the sum of the power in the frequency band is calculated and then divided by the number of frequency bins which lie in the frequency band for each ion species. The wavelet power is then divided by the frequency range for each ion species: $0.4f_{SC}$–$0.1f_{SC} = 0.3f_{SC}$. Points which lie within the cone of influence are discarded from the calculation. The cone of influence includes the red line and the red shaded area. It shows the region in the power spectrum which is potentially influenced by edge-effect artifacts. Points which lie above the Nyquist frequency were also discarded. The frequency averaged wavelet power over the $0.1f_{SC}$ and $0.4f_{SC}$ frequency band along time domain will be further called "wave power." The wave power of the magnetic field fluctuations at characteristic frequencies of each ion species is shown in Figure 2c.

The charge states of the ions affect the ion gyrofrequencies and therefore also the frequency band for the calculation of the wave power. JEDI does not provide information on the ion charge states. Clark et al. (2020) inferred the heavy ion charge states by analyzing energetic heavy ions accelerated by megavolt electric potentials. They propose that the charge states of energetic oxygen are primarily O^+ at large distances. The results are also consistent with the higher energy (about 100 keV/q) ion measurements from the Cassini flyby at the outer (about 200 R_J) post-dusk flank of the Jovian magnetosphere presented by Allen et al. (2019). Furthermore, Allen et al. (2019)

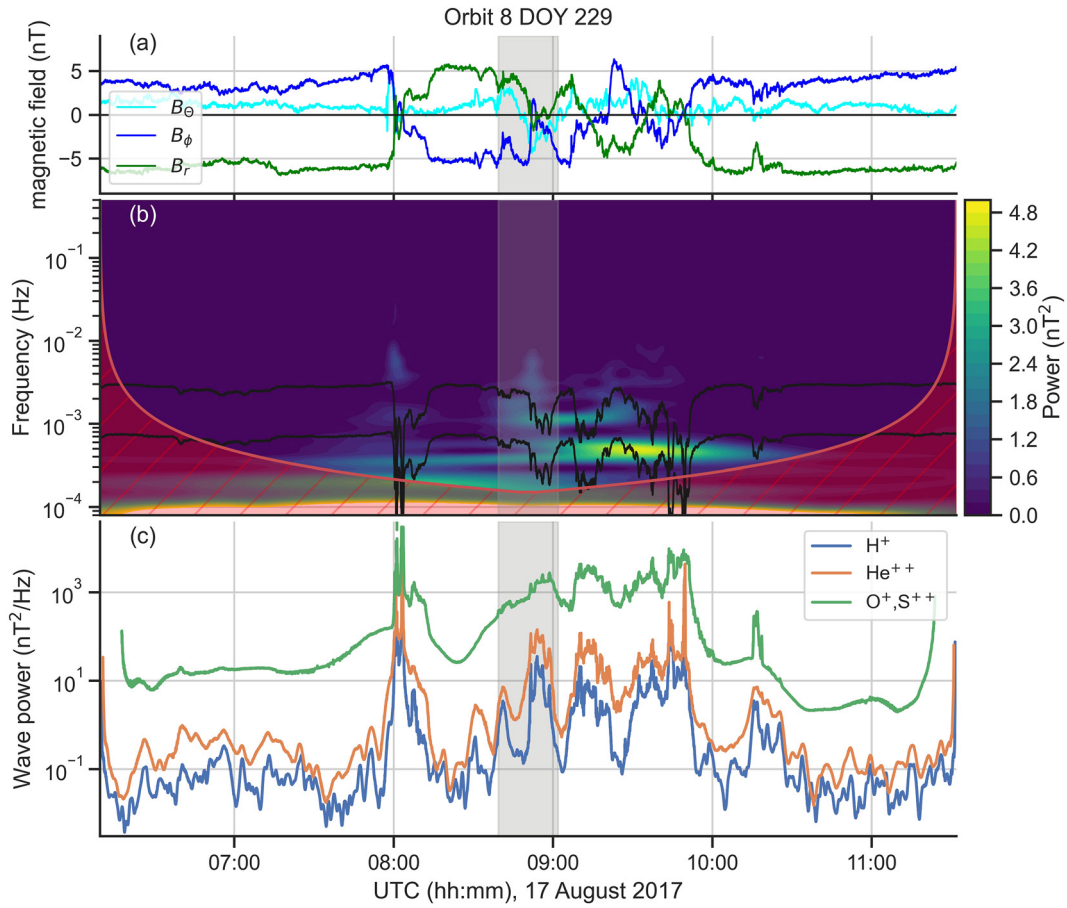

Figure 2. (a) Time series of the magnetic field components observed by Juno magnetometer. (b) Continuous wavelet power spectrum calculated from the wavelet analysis of B_ϕ fluctuations. Black lines on the wavelet power spectrum indicate the integration range at $0.1f_{SC}$ and $0.4f_{SC}$ for O^+ for the calculation of wave power. The cone of influence is indicated by the red line and the red hatched area. (c) Wave power of the magnetic field fluctuations at characteristic frequencies of each ion species for H^+, He^{++}, O^+, and S^{++}. Gray bars indicate the time of the plasmoid event.

showed that 25% of the energetic sulfur ions were S^+, 42% S^{++}, and 33% S^{+++}. Therefore, we use the same charge states of the heavy ions, O^+ and S^{++}, which were used by Kronberg et al. (2019) for the analysis of the wave power of the magnetic fluctuations at characteristic ion frequencies during the PM events.

4.2. Energy Spectral Index

The energy spectral index γ represents a slope of the ion energy spectrum $F_i \propto E_i^{-\gamma}$, where F_i is the ion flux and E_i is the energy of the ions. γ can be used to quantify the ion energy spectra and is calculated according to equation 6 in Kronberg and Daly (2013) by using the ion mean differential fluxes for two adjacent energy channels (F_{i1} and F_{i2}) and the effective energies which are approximated by the geometric mean between the lowest energies of the channels (E_{eff_1} and E_{eff_2}):

$$\gamma = \frac{\ln\left(F_{i1}/F_{i2}\right)}{\ln\left(E_{\text{eff}_2}/E_{\text{eff}_1}\right)}. \quad (1)$$

Since we are interested to see if energization of ions is present in the PMs, we look for a decrease of γ inside the PMs which is an indication for ion energization. In this study, we use ion intensity and ion mean differential flux synonymously.

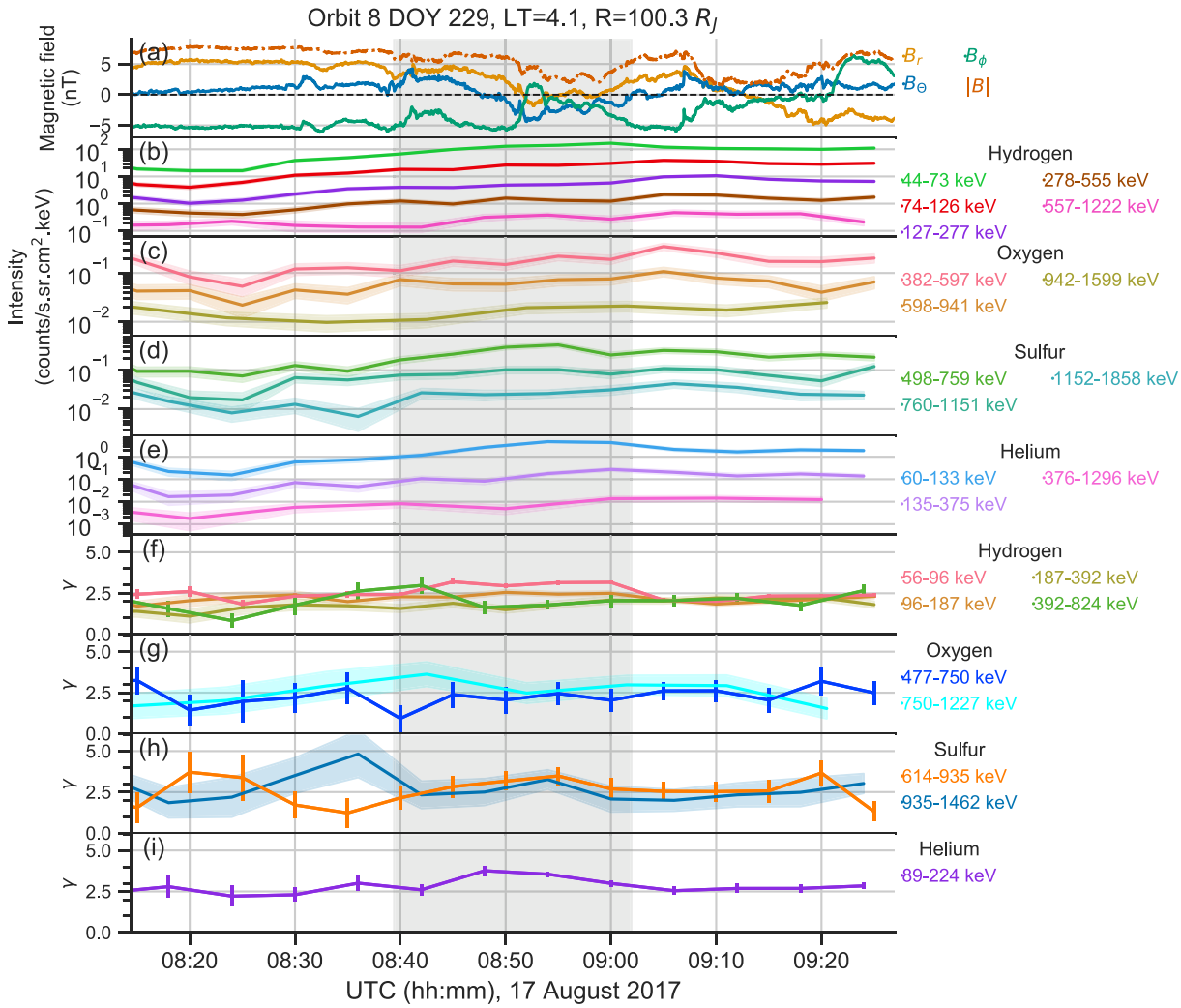

Figure 3. (a): JUNO magnetometer data of the magnetic field components during the plasmoid event on DOY 229 of 2017. (b–e): Ion intensities for hydrogen, oxygen, sulfur, and helium ions at different energy channels observed with Juno Energetic particle Detector Instrument. The intensities are averaged over a sampling interval which we adjust for each ion species and energy channel separately according to Section 4.3. For further information see text in Section 4.4. (f–i): Spectral index γ calculated from the ion intensities shown in (b–e) for different energy ranges. The energy ranges represent the geometric mean between the lowest energies of the neighboring channels. γ for helium ions at 224–698 keV was not calculated for this event because the relative error in helium ion intensity at 376–1296 keV (panel (e)) is above 30%. The bands and bars in panels (b–e) show the relative error obtained from the Poisson statistical error of the counts and in panels (f–i) the uncertainty in γ using error propagation of the errors in the ion intensities and Equation 1. Gray bars indicate the time of the plasmoid signature.

4.3. Time Resolution of the JEDI Data

In our analysis, the temporal resolution of the ion fluxes in each energy channel varies. We adjust the temporal resolution of the data so that no data gap is present in the time period of one PM event and that the relative error, which is obtained from the Poisson statistical error of the counts, is less than 30%. If both conditions can not be fulfilled we discard the data of the ion species and energy channel for the particular PM event. The temporal resolution of the ion intensity varies between 60 and 600 s with the most likely resolution above 300 s and the best resolution (≤200 s) for hydrogen ions in the lower energy channels (44–277 keV).

4.4. Plasmoid Event on 17 August 2017

In Figure 3 we present the magnetic field data (panel (a)) and ion intensity data (panels (b)–(e)) of a plasmoid event from orbit 8 on day 229 of 2017, when Juno was located at a radial distance of about 100 R_J from Jupiter. The plasmoid can be recognized by the bipolar fluctuation in the meridional magnetic field component shown by

the blue line in the first panel, which resembles a magnetic signature during a tailward-moving plasmoid. B_θ is positive and experiences an increase relative to the background B_θ at 08:39 UTC, then crosses zero and becomes negative. About 14 min after the zero crossing B_θ becomes positive again. The plasmoid starts at 08:39 UTC and lasts for about 23 min. The time interval of the plasmoid is indicated by the gray bars. The magnitude of the radial component of the magnetic field (B_r) and the total field magnitude decrease after the zero crossing in B_θ at about 08:49 UTC, suggesting a magnetic loop structure. B_r is mostly positive and experiences a short reversal during the PM from 08:51 to 08:59 UTC which indicates that Juno approached the current sheet center from the northern part of the current sheet. Figures 3b–3e show ion intensities at different energy ranges (44–1222 keV for hydrogen, 382–1599 keV for oxygen, 498–1858 keV for sulfur, and 60–1296 keV for helium). A gradual increase of the ion intensities can be observed already before the start of the PM (08:25 UTC) in most of the energy ranges. Most of the intensities remain enhanced also after the end of the PM.

The JEDI data shown in Figures 3b–3e is time averaged over a time interval between 300 and 600 s. We adjust a sampling interval for each ion species and energy channel separately so that it fulfills the conditions described in Section 4.3. It is visible that the relative error of the intensity for the ions of higher energies is larger compared to the ions of lower energies. Intensity of hydrogen ions at 44–73 keV for this event and temporal resolution of 300 s has an average relative error of 7% whereas intensity of hydrogen ions at 557–1222 keV with temporal resolution of 360 s has an average relative error of 28%. The intensity of helium ions at 376–1296 keV time averaged over 600 s shown in panel (e) does not fulfill the conditions from Section 4.3 because of an average relative error of 37% and will therefore be discarded for the statistical analysis.

Panels (f)–(i) of Figure 3 display the time profiles of the energy spectral index γ for hydrogen, oxygen, sulfur, and helium ions. Due to the large error bars a trend in the energy spectral index for most of the ions and energy ranges can't be resolved in this example. A slight decrease of γ is visible in the hydrogen ions at 392–824 keV and oxygen ions at 477–750 keV inside the PM. γ for helium ions at 89–224 keV increase during the PM.

The wavelet analysis for this event is shown in Figure 2. The wave power shows fluctuations at frequency bands corresponding to H^+ of several orders of magnitude during the PM (blue line in (c)). The wave power of the magnetic field fluctuations during the PM at frequency bands corresponding to O^+ and S^{++} (about $3 \cdot 10^2$–$3 \cdot 10^3$ nT^2/Hz) is larger than those at frequency bands corresponding to H^+ and He^{++} (about 10^{-1}–10^2 nT^2/Hz). This is because the frequency bands for H^+ and He^{++} are higher in the wavelet power spectrum due to larger ion gyrofrequencies and the fluctuations of the power in the scalogram (see Figure 2b) are mostly located below 10^{-2} Hz. Comparing the wave power in the time interval before the start of the PM signature (08:14–08:39 UTC) and during the PM signature (gray bar), the wave power at all frequency bands starts to increase about 10 minutes before the PM signature and reaches a local maximum inside the PM signature.

5. Results: Plasmoid Statistical Studies

In this section we present the results from the statistical analysis.

5.1. Ion Intensities and Wave Power During Plasmoid Events in the Vicinity of the Current Sheet Center

Kronberg et al. (2019) analyzed Galileo observations and showed that the intensity of heavy ions inside plasmoids is strongly increased close to the current sheet center which indicates that the ions were accelerated inside the plasmoids. Following Kronberg et al. (2019), we investigate if an increase is visible in the ion intensities observed in selected plasmoids relative to the ion intensities observed before the start of the plasmoids in the vicinity of the current sheet center. In the current sheet center the magnetic field component B_r is equal to zero and we use $|B_r|$ as an indicator for the location of the spacecraft relative to the current sheet center during the PM observations. In order to compare the ion intensities to the magnitude of B_r we resample $|B_r|$ so it has the same time resolution as the ion fluxes. Then, we define bins of a bin width of 2 nT for the magnitude of B_r and distribute the ion intensities in the bins. We calculate the mean of the ion intensities in each bin for time intervals of 25 min before the start of the plasmoids and during plasmoids. We choose the time interval of 25 min in order to have at least three measurements of ion fluxes from each PM event.

To quantify the increase of the ion intensity during plasmoids we introduce the factor $\alpha = \overline{I}_{\text{inside, 0-2 nT}} / \overline{I}_{\text{before, 0-2 nT}}$ which is the relation between the mean of the ion fluxes inside $\left(\overline{I}_{\text{inside, 0-2 nT}}\right)$ and before the start of the PM

Table 1
Relation α Between the Mean of the Ion Fluxes Inside and Before the Start of the Plasmoids (PMs) Close to the Current Sheet Center and the Number of PM Events Used for the Statistical Analysis for Different Cases

	All PMs[a],[b]	Total events[c]	$R < 100\ R_J$ ($R \geq 100\ R_J$)[a]	Total events[c]	LT > 4(LT≤ 4)[a]	Total events[c]	85° ≤ θ ≤ 95° (85° > θ < 95°)[a]	Total events[c]	ϕ > 100° (ϕ ≤ 100°)[a]	Total events[c]
Oxygen										
382–597 keV	**1.8**	27	**2.6** (0.7)	14 (11)	**2.2** (1.2)	16 (9)	**3.5** (1.3)	9 (16)	**2.0** (1.2)	10 (15)
598–941 keV	1.2	25	**2.6** (0.4)	15 (10)	**1.9** (0.8)	15 (10)	**3.9** (0.9)	9 (16)	**2.0** (0.6)	11 (14)
942–1599 keV	0.8	20	**2.9** (0.2)	15 (5)	**2.8** (0.5)	12 (8)	**2.5** (0.6)	9 (11)	**1.6** (0.3)	7 (13)
Sulfur										
498–759 keV	**2.8**	31	**2.5** (**1.9**)	15 (14)	**2.9** (**1.6**)	18 (11)	**2.8** (**2.1**)	12 (17)	**2.3** (**2.2**)	11 (18)
760–1151 keV	**2.0**	28	**2.6** (1.2)	15 (12)	**2.0** (1.2)	17 (10)	**1.8** (1.4)	12 (15)	**1.7** (**1.7**)	10 (17)
1151–1858 keV	**1.5**	26	**2.8** (0.5)	15 (10)	**2.6** (0.8)	15 (10)	**3.2** (1.0)	10 (15)	**2.1** (1.0)	10 (15)
Helium										
60–133 keV	**2.0**	29	**1.6** (**1.7**)	15 (14)	**1.9** (1.1)	18 (11)	**1.5** (**1.6**)	12 (17)	**3.5** (1.4)	10 (19)
135–375 keV	1.1	25	**1.6** (0.7)	14 (12)	1.1 (0.6)	16 (10)	1.0 (0.6)	10 (16)	**1.8** (1.0)	10 (16)
376–1296 keV	0.3	14	−(0.1)	11 (3)	−(0.1)	8 (6)	−(0.2)	7 (7)	−(0.2)	3 (11)
Hydrogen										
44–73 keV	1.1	31	0.8 (0.9)	16 (15)	0.9 (0.6)	19 (12)	0.8 (0.8)	13 (18)	**1.7** (0.9)	12 (19)
74–126 keV	1.2	31	1.1 (0.9)	16 (15)	1.1 (0.7)	19 (12)	1.0 (0.8)	13 (18)	1.0 (1.1)	12 (19)
127–277 keV	1.1	31	1.0 (1.0)	16 (15)	0.9 (0.7)	19 (12)	0.9 (0.9)	13 (18)	0.7 (1.0)	12 (19)
278–555 keV	**1.7**	27	**2.0** (0.9)	14 (11)	**1.9** (0.6)	18 (7)	**1.9** (0.9)	12 (13)	0.9 (1.3)	10 (15)
557–1222 keV	**1.5**	15	**2.1** (0.6)	11 (4)	−(0.6)	7 (8)	−(0.9)	5 (10)	**1.6** (0.6)	6 (9)

[a]α for different cases. Significant increase of ion intensities inside plasmoids is considered when α ≥ 1.5 (marked in bold font). [b]This case considers the statistical analysis of all identified plasmoids. [c]Total number of events which were used for the statistical analysis in each case. The number depends on the conditions mentioned in Section 4.3.

$\left(\overline{I}_{\text{before, 0–2 nT}}\right)$ in the 0–2 nT $|B_r|$-bin. For the calculation we take the upper (lower) limit of the 95% confidence interval of $\overline{I}_{\text{before, 0–2 nT}}$ and the lower (upper) limit of the 95% confidence interval of $\overline{I}_{\text{inside, 0–2 nT}}$ if $\overline{I}_{\text{before, 0–2 nT}} < \overline{I}_{\text{inside, 0–2 nT}}$ $\left(\overline{I}_{\text{before, 0–2 nT}} > \overline{I}_{\text{inside, 0–2 nT}}\right)$ for each ion species at each energy range. The 95% confidence interval indicates that there is a 95% probability that the true mean of the data sample is included in the range of the confidence interval. We use the bootstrapping method (Efron & Tibshirani, 1994) to calculate the confidence interval from the data sample. The factor α represents the minimal increase of the ion intensities in the PMs and is displayed for different classification cases in Table 1. If the confidence intervals of the ion intensities before the PMs and inside the PMs overlap then $\alpha < 1.0$. We consider a significant enhancement of ion intensity close to the current sheet center when $\alpha \geq 1.5$. The first column of Table 1 shows the calculated α for oxygen, sulfur, helium, and hydrogen ions at different energy ranges for the 31 identified PM events denoted by "all PMs." Our aim is to examine how the location of the identified PM events in the Jovian magnetotail, such as the radial distance to Jupiter or the latitudinal distribution, affects the ion intensities inside the PMs close to the current sheet center. Therefore, we divide our study into different cases and analyze the selected PMs in these special cases: (a) The radial distance R between the PMs and Jupiter is smaller (larger) than 100 R_J, (b) Local time of the observations is before (after) 04:00 LT, (c) The PM events are located close to the jovigraphic equator (colatitude $85° < \theta < 95°$), (d) The PM events are located at different longitudes. The longitudinal position indicates the direction of the spacecraft crossing the current sheet center (see K. K. Khurana & Schwarzl, 2005). The factor of minimum increase of different ion intensities and the number of events which were used for the statistical analysis for each case are shown in Table 1.

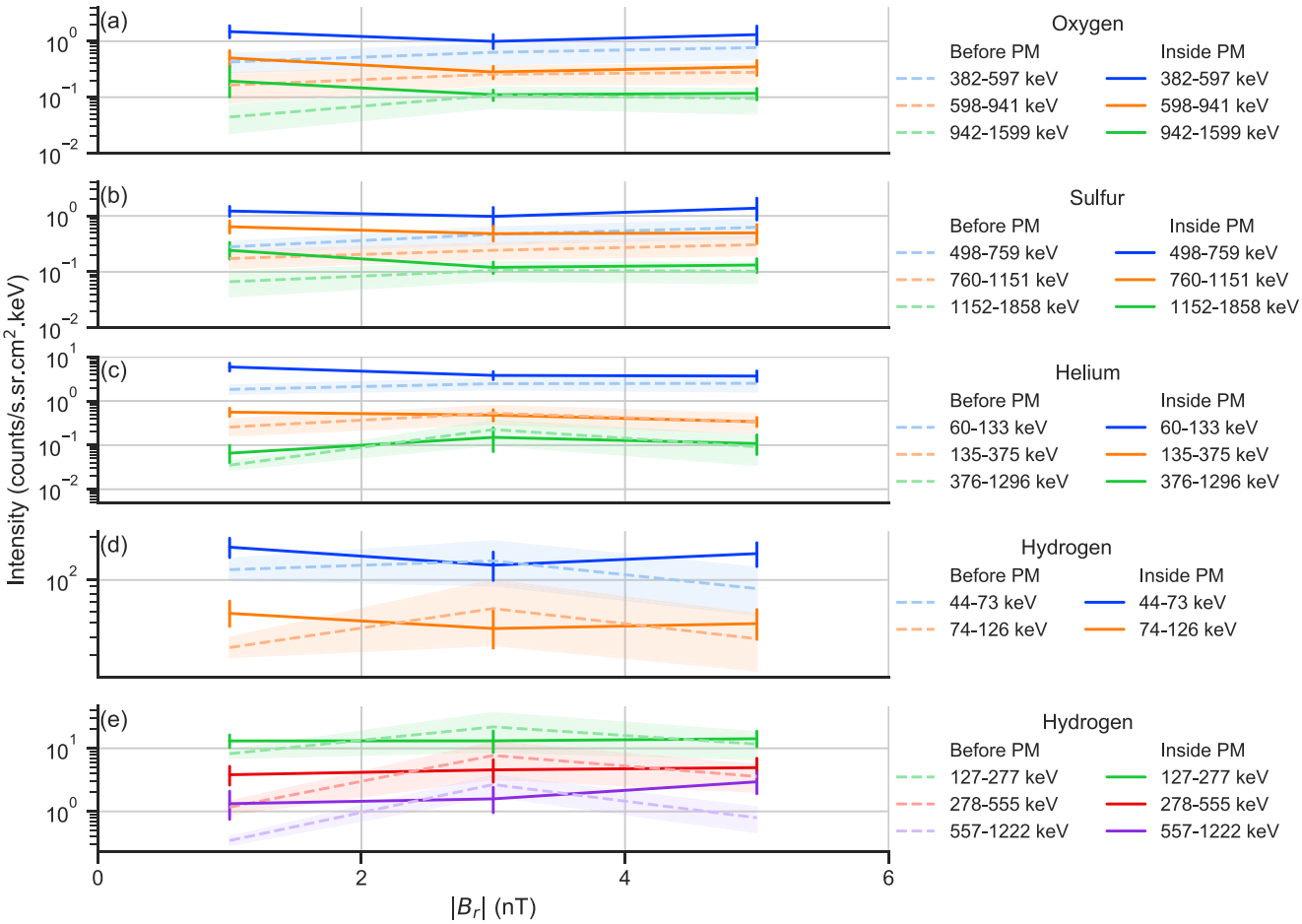

Figure 4. Statistical survey of 31 plasmoid (PM) events showing the dependence of the intensity of oxygen (a), sulfur (b), helium (c), and hydrogen ions (d) and (e) on the position of the spacecraft with respect to the current sheet represented by $|B_r|$. $|B_r|$ is approximately zero in the center of the current sheet and becomes larger with the distance from the center of the current sheet. Solid lines represent the ion intensity during the PMs and dashed lines the ion intensity in the time period of 25 min before the start of the PMs. Colored bands and bars indicate the 95% confidence interval in the time period of 25 min before the start of the PM and during the PM, respectively.

5.1.1. Oxygen, Sulfur, and Helium Ion Intensities

The results of the statistical analysis of the 31 PM events are shown in Figure 4. The minimal increase of the ion intensities inside the plasmoid structures is quantified by α and is shown in the first column of Table 1 for all PM events. The comparison between the ion intensities detected during the PMs (solid lines including error bars) and before the start of the PMs (dashed lines including error bands) revealed a significant enhancement of the intensities of the heavy ions, that is, oxygen ions at 382–597 keV and sulfur ions, inside the PMs close to the current sheet center ($|B_r| < 2$ nT) shown in Figures 4a and 4b. The increase inside the PMs is larger for oxygen and sulfur ions in the lower energy ranges (<600 keV for O and <760 keV for S) than in the upper energy ranges (see Table 1). The oxygen ion intensities at the energy range of 382–597 keV are increased by an average factor of 1.8 inside the PMs compared to those before the PMs and the sulfur ion intensities at 498–759 keV are increased by a factor of 2.8. Farther away from the current sheet center ($|B_r| > 2$ nT) no conclusion can be made about a significant increase or decrease of the intensities in all ion species and at all energy ranges inside the 31 PMs because the error bars overlap (see Figure 4). Helium ion intensities in the energy range of 60–133 keV are increased by a factor of two inside the PMs. Comparing the different classification cases in Table 1, it is visible that the increase of sulfur and oxygen ion intensities inside the PMs is prominent in PMs with a radial distance less than 100 R_J to Jupiter, in PMs close to the jovigraphic equator, and PMs which were observed after 04:00 LT. About 85% of the PM events close to the jovigraphic equator were observed after 04:00 LT in a radial distance less than 100 R_J. For the case of the PM events observed after 04:00 LT about 63% of the events were located in a radial distance less

than 100 R_J and 68% of the events were located close to the jovigraphic equator. A significant increase of the ion intensities in the PMs is also observed for PM events which were detected at longitudes larger than 100°. In this region we observed most of the south to north crossings where the spacecraft moves from the south of the current sheet to its north which is indicated by the change of B_r from a negative value to a positive value. The longitudinal location of the south to north (north to south) crossings of the current sheet is in accordance with the study of Khurana and Schwarzl (2005) (see their figure 13).

An enhancement of the helium ion intensities at 60–133 keV and at 135–375 keV is observed in several cases. The results indicate that the heavy ions and helium ions are accelerated inside PMs and that the observed effectiveness of the acceleration is dependent on the position of Juno during the plasmoid event.

5.1.2. Hydrogen Ion Fluxes

The statistical analysis of different classification cases revealed that a significant increase of the hydrogen ion intensities in the PMs is not observed in the energy ranges 74–277 keV (see Table 1). Taking the error bars into account, this is also visible in Figures 4d and 4e (orange and green lines) where no intensity increase of protons inside the PMs is observed in these energy ranges. We observe a significant enhancement of the hydrogen ion intensities at 278–555 keV and 557–1222 keV inside the PMs (see first column of Table 1). The most prominent increase is visible in the hydrogen ion intensities at 278–555 keV for 14 and at 557–1222 keV for 11 PMs observed in a radial distance less than 100 RJ from Jupiter (see third column of Table 1).

5.1.3. Energy Spectral Index

The analysis of the distribution of the observational probability of the energy spectral index γ for different ion species and energy ranges observed in the time interval of 25 min before the PM signatures and inside the PM signatures does not reveal a significant difference. Also no significant differences in the γ values are seen between the light and heavy ions.

At several events a decrease of γ inside the PM, which indicates the energization of the ions, is detected at different times for different energy ranges of the ions. In order to calculate in how many PM events a decrease of γ is observed, we take the minimum values of γ in the time interval of 25 min before the PM signatures ($\gamma_{\text{before, min}}$) and the minimum values of γ inside the PM signatures ($\gamma_{\text{P,min}}$). In Figure 5 we show the distribution of the observational probability of $\gamma_{\text{P,min}}$ and $\gamma_{\text{before, min}}$ for different ion species and energy ranges. For sulfur ions at 614–935 keV the probability is high to observe $\gamma_{\text{P,min}} \leq 1$ (see Figure 5b). Since the probability is smaller to observe an energy spectral index in this range before the PM signature ($\gamma_{\text{before, min}}$), the results indicate that sulfur ions at 614–935 keV are energized inside some of the PMs.

Although the probability to observe $\gamma_{\text{P,min}}$ in the range of 1 and 2 is higher than the probability for $\gamma_{\text{before, min}}$ for oxygen ions at 477–750 keV, the results are not as obvious as for sulfur ions at 614–935 keV. The lighter ions do not clearly show that the probability is higher to observe smaller values of $\gamma_{\text{P,min}}$ than of $\gamma_{\text{before, min}}$ (see Figures 5c and 5d). We consider a significant decrease of γ inside the PM when $\gamma_{\text{P,min}}/\gamma_{\text{before, min}} < 0.8$. Following this criterion, a decrease of γ at some point inside the 31 PMs was observed in about 29% of the events for oxygen ions, in about 53% (40%) of the events for sulfur ions at 614–935 keV (935–1642 keV), in 35% (29%) of the events for helium ions at 89–224 keV (224–698 keV), in 35% of the events for hydrogen ions at 56–96 keV, in 19% of the events for hydrogen ions at 96–187 keV, in 20% of the events for hydrogen ions at 187–392 keV, and in 21% of the events for hydrogen ions at 392–824 keV.

5.2. Relation Between Ion Intensities, Energy Spectral Index and Wave Power

5.2.1. Intensities Versus Wave Power

In Figure 6 we show the dependencies of the intensities for oxygen, sulfur, helium and hydrogen ions at different energies on the wave power during the time of the observed PM signatures. The observed intensities (blue circles) are broadly scattered in the plots. To get a better idea of the trend in the data we apply a non-parametric smoother (LOESS) (Cleveland & Devlin, 1988) shown by the cyan line. The first and second columns of Figure 6 show the oxygen and the sulfur ion intensities in dependence on the wave power of the magnetic fluctuations at characteristic frequencies corresponding to the gyrofrequencies of O^+ and S^{++}, respectively. The heavy ion intensities at the energy ranges <942 keV for oxygen and <1858 keV for sulfur ions start to increase with wave power for

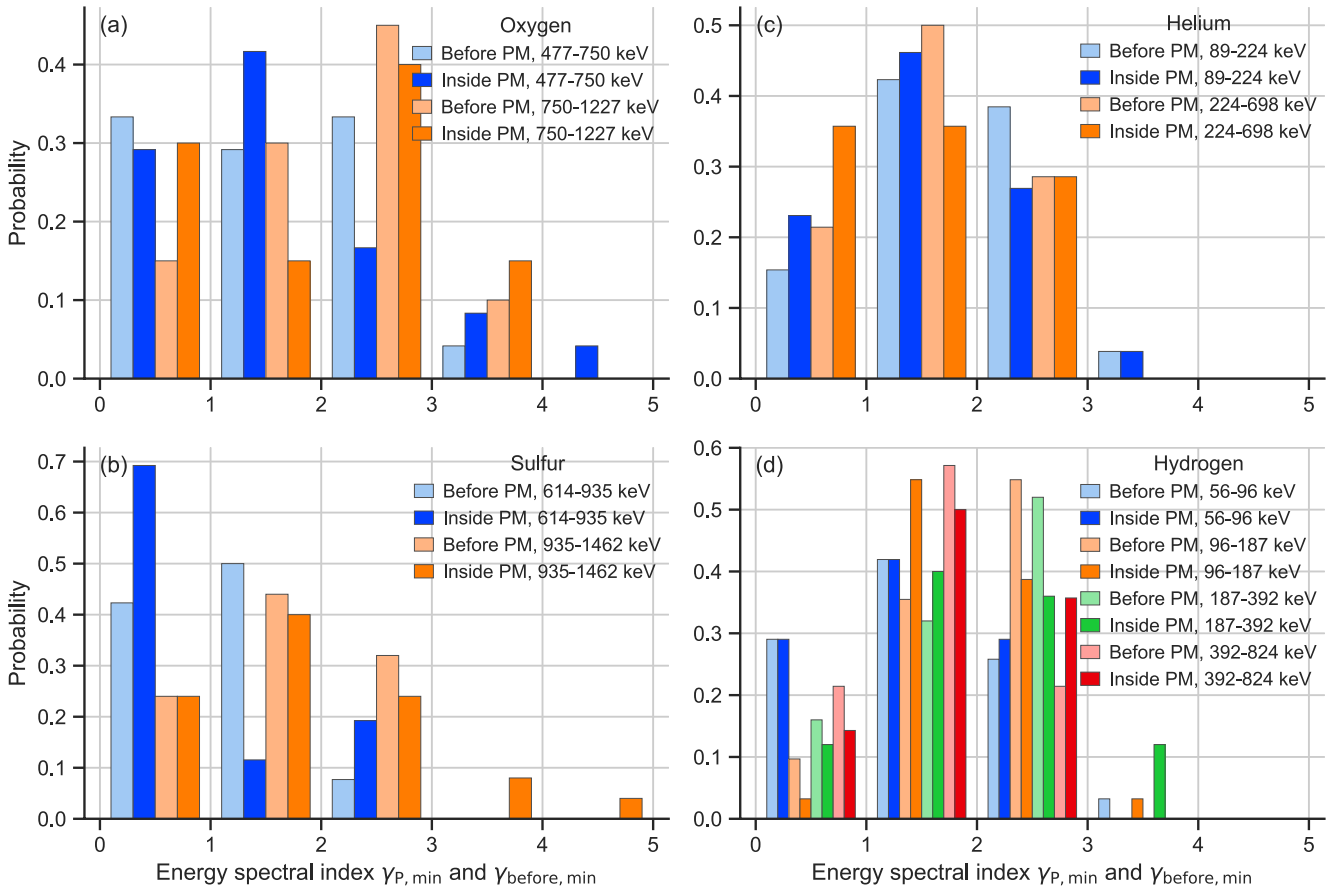

Figure 5. Distribution of the observational probability of the minimum energy spectral index $\gamma_{P,min}$ inside the plasmoids (PMs) (shown by darker colors) and the minimum energy spectral index $\gamma_{before,\,min}$ before the start of the PMs (shown by lighter colors) for different ion species and energy ranges. The distribution is shown for the 31 PM events. The energy ranges displayed in the histograms are the geometric means between the lowest energies of the neighboring channels.

wave powers larger than 10 nT^2/Hz until 300 nT^2/Hz. Most of the observed oxygen and sulfur data points lie in the wave power range between 10^2 and 10^3 nT^2/Hz whereas the observed helium and hydrogen data points are not confined to a wave power range (seen in Figures 6 and 7). Intensities of hydrogen ions at 44–73 keV and 557–1222 keV (not shown here) follow a similar distribution with wave power as hydrogen ions at 74–126 keV and 278–555 keV, respectively. The spread of the data points of the intensity for hydrogen ions with wave power is broader (as seen in the right column of Figure 6) than for the heavy ions. However, a slight increase of intensities of helium ions at energies <375 keV and hydrogen ions at energies <126 keV with wave power is visible. The wave power range at characteristic frequency bands for the heavy ions (about 1–7,000 nT^2/Hz) is significantly higher than that for the light ions (about 10^{-3}–100 nT^2/Hz for H^+ and 10^{-2}–300 nT^2/Hz for He^{++}). Therefore, we expect the energization of heavy ions to be more effective due to the resonant interaction with magnetic field fluctuations than that of light ions.

5.2.2. Spectral Index Versus Wave Power

In Figure 7 we show the dependencies of the ion energy spectral index γ at different energies on the wave power at frequencies corresponding to the ion gyrofrequencies during the time of the observed plasmoid structures. The spectral index was calculated with Equation 1 and the geometric mean of the energy ranges used for the calculation of γ is indicated in Figure 7. The spectral index is broadly spread. γ for all ion species and energy ranges does not show a correlation with the wave power.

The reason that we do not observe a correlation between the energy spectral index and wave power might be the coarse time resolution of our data. Especially fast accelerated hydrogen ions quickly leave the PM as shown by the modeling in Kronberg et al. (2019).

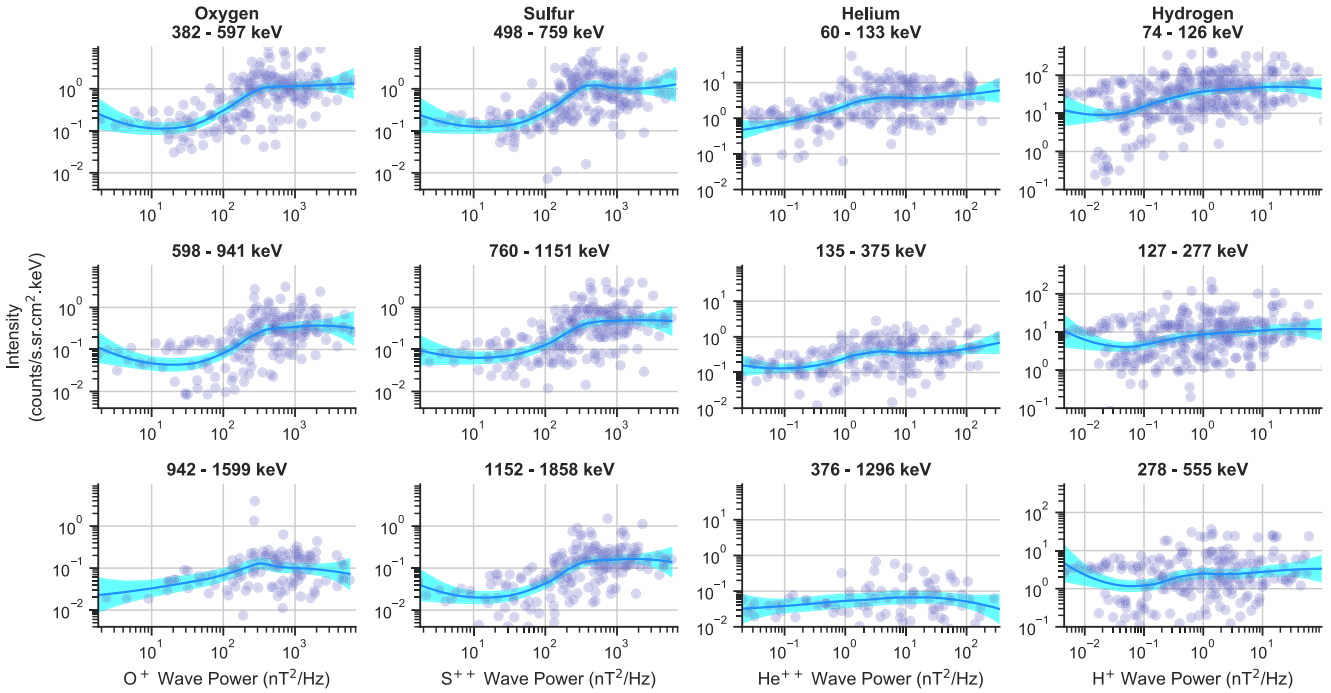

Figure 6. Dependencies of the ion intensities at different energy ranges on the wave power at characteristic frequency bands for O^+ (first column), S^{++} (second column), He^{++} (third column), and H^+ (fourth column) for 31 plasmoids. The observed fluxes are shown as blue filled circles. The cyan line shows the locally estimated scatterplot smoothing method (LOESS) with 95% confidence intervals fitted to the observed fluxes.

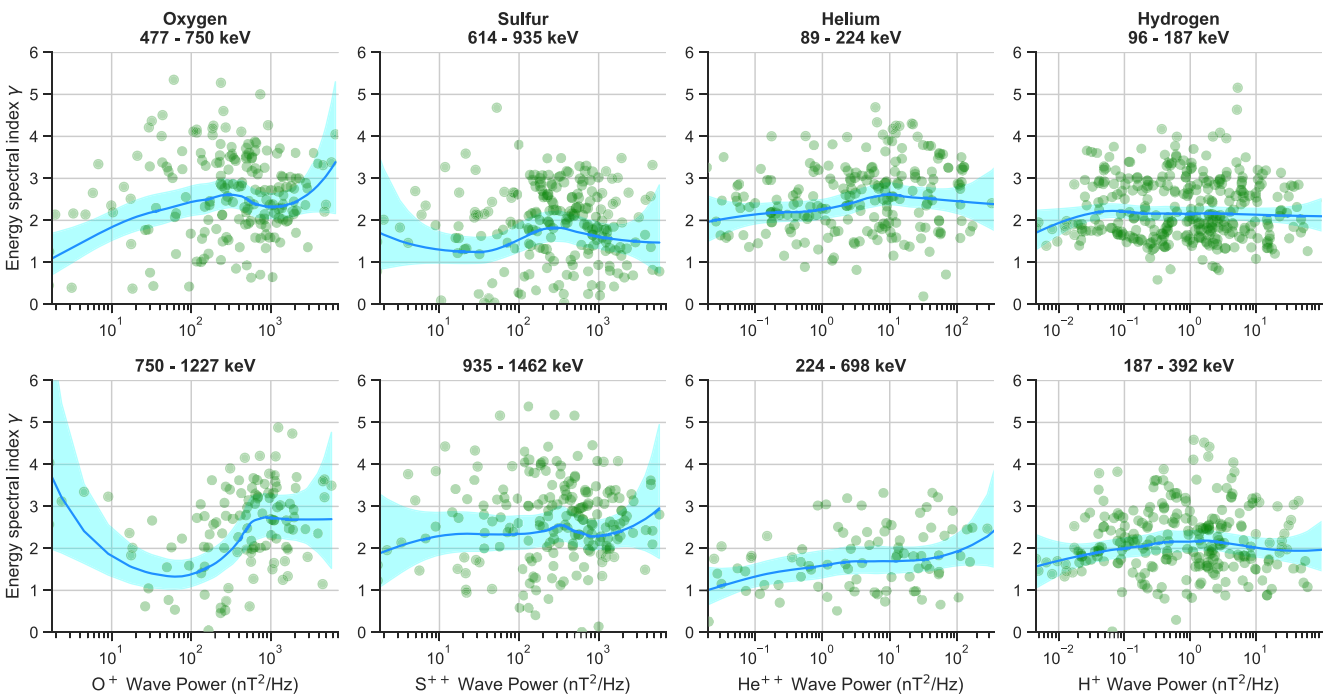

Figure 7. Dependencies of the energy spectral index γ on the wave power at characteristic frequency bands for O^+ (first column), S^{++} (second column), He^{++} (third column), and H^+ (fourth column) for 31 plasmoids. The energy ranges are the geometric means E_{gm} of two neighboring channels. The calculated γ is shown as green filled circles. The cyan line shows the locally estimated scatterplot smoothing method curve with 95% confidence intervals fitted to the observed energy spectral index.

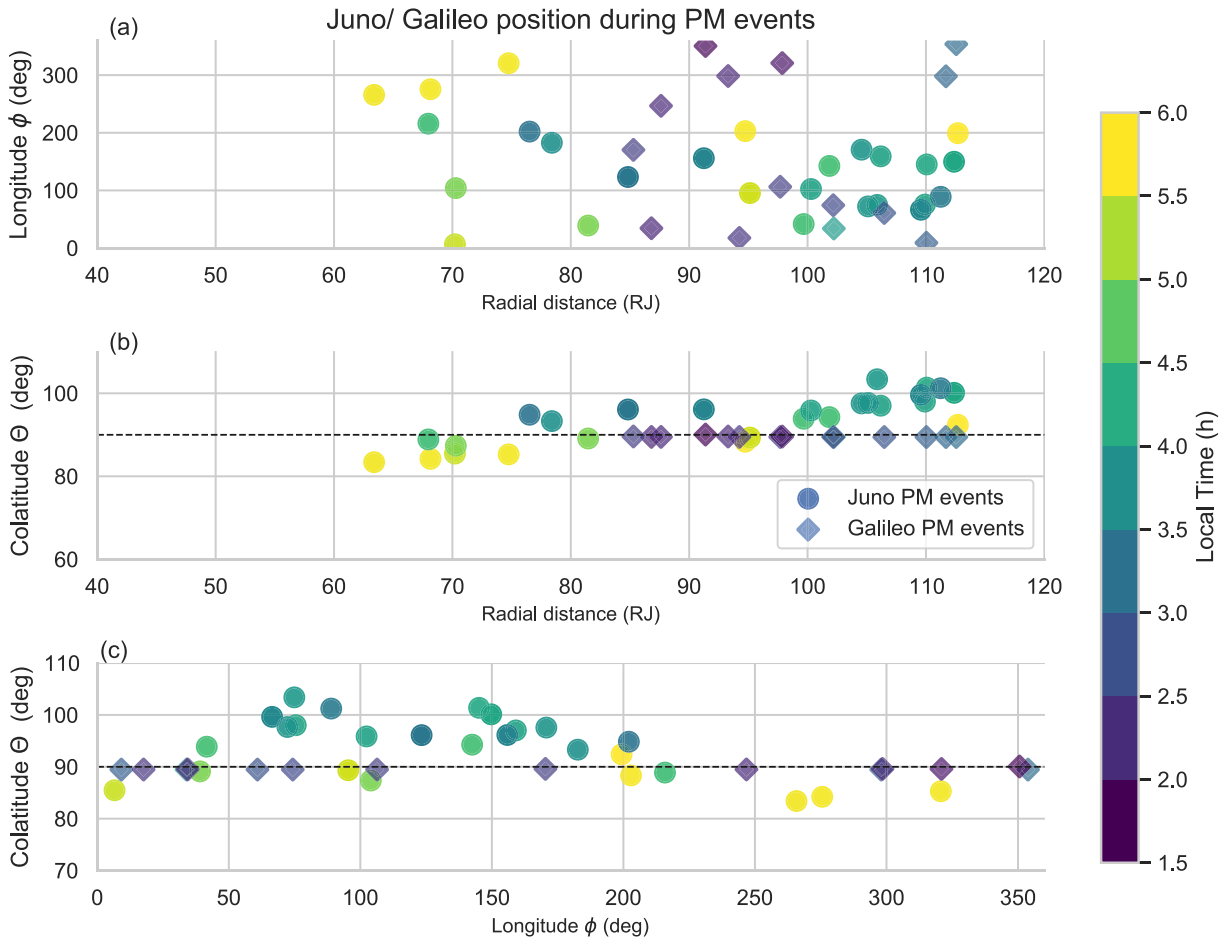

Figure 8. Position of the Juno (circles) and Galileo (diamonds) spacecrafts during plasmoid (PM) events in the right-handed System III coordinates. The diamonds show the locations of the PM events analyzed in the study of Kronberg et al. (2019). The colorbar gives information on the local time of each PM event. Dashed lines indicate the position of the jovigraphic equator.

5.3. Comparison With Results From Galileo Observations

Kronberg et al. (2019) analyzed 14 PM events which were identified in the Galileo observations. The distribution of the PM events observed with Galileo differs from those observed with Juno (see Section 3.1). The locations of these 14 events are shown in the diamond shapes in Figure 8. All 14 events were located very close to the jovigraphic equator in a radial distance to Jupiter between 85 and 115 R_J. The events were observed between 01:15 and 04:00 local time with most of them at around 02:20 LT. In the study of Kronberg et al. (2019), the comparison between the sulfur and oxygen ion intensities during PMs and the ion intensities 25 min before PMs showed a statistically significant increase of ion intensities during PMs not only close to the current sheet center but also farther away (up to B_r = 7 nT). The ion intensities for oxygen in the energy range of 51–112 keV/nuc (about 816–1,792 keV) and sulfur in the energy range of 62–310 keV/nuc (about 1984–9,920 keV) were increased by a factor of 2 close to the current sheet center. Hydrogen ions at 345–822 keV/nuc did not show a change in the ion intensities before and during the plasmoids close to the current sheet center.

We analyzed Juno observations of oxygen ions at energies between about 380 and 1600 keV and sulfur ions at energies between about 500 and 1,860 keV. Compared to the study of Kronberg et al. (2019), we observe a larger increase in the ion intensities for oxygen in the energy range of 942–1,599 keV and sulfur in the energy range of 1,151–1,858 keV close to the current sheet center for the case of PM events located close to the jovigraphic equator (see Table 1). However, only 13 PM events were located close to the jovigraphic equator and due to limitations of the time resolution we used only 9 PM events for the statistical analysis of oxygen ions in the energy range of 942–1,599 keV and 10 PM events for the statistical analysis of sulfur ions in the energy range of

1,151–1,858 keV. Furthermore, we see an increase of hydrogen ion intensities by a factor of about 2 in the energy range of 278–555 keV close to the current sheet center.

Kronberg et al. (2019) concluded that plasmoids with higher electromagnetic turbulence lead to stronger acceleration of oxygen and sulfur ions. They showed a nonlinear increase of heavy ion intensities and a decrease of the energy spectral index with wave power of the B_θ magnetic field fluctuations at the frequency ranges corresponding to gyrofrequencies of the O^+ and S^{++} ions. Oxygen intensities at all observed energy ranges from 26 to 562 keV/nuc (about 416–8,990 keV) and sulfur intensities at 62–310 keV/nuc (about 1,984–9,920 keV) started to increase from wave power in the order of 10 nT^2/Hz. Although we calculated the wave power from B_ϕ in our study and not from the north-south magnetic field component as Kronberg et al. (2019), we also see an increase of the oxygen and sulfur ion intensities from wave power >10 nT^2/Hz corresponding to gyrofrequencies of the O^+ and S^{++} ions (see Figure 6). However, Kronberg et al. (2019) showed that sulfur intensities at lower energies 30–62 keV/nuc (960–1,984 keV) start to increase from wave power >1 nT^2/Hz at corresponding S^{++} gyrofrequency band. A decrease of the energy spectral index of the heavy ions with wave power at corresponding O^+ and S^{++} gyrofrequency ranges is not visible in our observations and therefore a conclusion how the electromagnetic turbulence affects the energization of heavy ions during the PMs is not possible.

Test particle simulations performed by Kronberg et al. (2019) yielded that electromagnetic turbulence in plasmoids plays an essential role in the acceleration of hydrogen, oxygen, and sulfur ions. In both studies derived from Galileo and Juno observations, a significant increase of intensity and decrease of energy spectral index of hydrogen ions at all analyzed energy channels are not correlated with wave power. The modeling in Kronberg et al. (2019) showed that the fast accelerated protons quickly leave the plasmoid and therefore a correlation of hydrogen ions with the wave power might not be visible due to the time and energy resolution of the data. The protons are accelerated due to electromagnetic fluctuations during the first 150 s. The time resolution of the fluxes measured with Galileo vary between 180 and 660 s whereas the time resolution of the fluxes measured with Juno vary between 60 and 600 s in our study with the most probable time resolution >200 s. Therefore, the time resolution of the Juno data might also be too coarse in order to observe acceleration effects of the hydrogen ions in the energies <1,222 keV due to electromagnetic turbulence. The most probable energy to be observed during a time interval of 200 s according to simulations is higher than the energy range analyzed here (>2 MeV) (see Kronberg et al., 2019). Although simulations suggest that O^+ resonantly interacts with electromagnetic fluctuations during a time period of 400 s (see figure 9 in Kronberg et al., 2019), a change of the energy spectral index with wave power is not visible in our data. The S^{++} ions are resonantly accelerated during the first 50 s and then leave the plasmoid quickly because of their large gyroradii (see figure 9 in Kronberg et al., 2019). Their most probable energy to be observed is larger than the energy of the sulfur ions we analyze in this study.

6. Summary and Conclusions

In this study we used Juno's MAG and JEDI observations and investigated the effectiveness of ion energization and acceleration in plasmoids in the Jovian magnetotail and how the ion acceleration inside the plasmoids is affected by the location of the plasmoids. In the MAG data of Juno's first 16 orbits of Jupiter (July 2016–October 2018) we identified 31 plasmoid events which were close to the current sheet center during the plasmoid signature and were embedded in a quiet magnetic field environment. We have examined the statistical properties of oxygen (382–1,599 keV), sulfur (498–1,858 keV), helium (60–1,296 keV), and hydrogen (44–1,222 keV) ions inside the plasmoids and in a time interval of 25 min before the start of the plasmoids similar to the study of the plasmoids detected in Galileo data by Kronberg et al. (2019). We analyzed the relation between the ion intensity, wave power, energy spectral index and the distance from the current sheet center during the plasmoid events. Our statistical analysis yielded the following results:

1. Intensities of heavy ions were more likely to be enhanced close to the current sheet center in the PMs than those of the lighter ions. The enhancement of heavy ion and hydrogen ion intensities at 278–1,221 keV inside the plasmoids compared to the ion intensities before the start of the plasmoids was prominent in PMs which were detected in a radial distance less than 100 R_J to Jupiter, close to the jovigraphic equator, and after 04:00 LT. At lower energy ranges (44–277 keV) the hydrogen ions did not show a significant increase. Furthermore, a significant increase of heavy ion intensities was observed in PMs which were identified at longitudes larger than 100°, where the spacecraft moved from the southern part to the northern part of the current sheet.

Intensities of helium ions in the energy range of 60–133 keV were increased by a factor of about two inside the PMs close to the current sheet center. The results indicate the acceleration of heavy ions, helium ions at 60–375 keV and hydrogen ions at 278–1,222 keV inside PMs with the observed efficiency of the acceleration being dependent on the location and local time of the PMs.

2. A significant decrease of the energy spectral index inside the PMs was observed in more than 50% of the PM events for sulfur ions at 614–935 keV while only in about 20% of the events a decrease of γ was observed for hydrogen ions at energies >96 keV.
3. An increase of the heavy ion intensities with wave power at energy ranges <942 keV for oxygen and <1,858 keV for sulfur ions inside the PMs was shown for wave power >10 nT^2/Hz whereas no significant increase of ion intensities with wave power was seen for helium and hydrogen ions.
4. No correlation was visible between the wave power and the energy spectral index for all ion species and energy ranges inside the PMs. Therefore, no conclusions can be made here about the nonadiabatic ion acceleration as a consequence of resonant interactions with the magnetic field fluctuations as it was shown for heavy ions in plasmoids observed with Galileo by Kronberg et al. (2019).

The time resolution of the fluxes might be too coarse for the investigation of the influence of the magnetic field turbulence on the acceleration of ions during the PMs. Further investigations are required on how electromagnetic turbulence affects ion acceleration inside plasmoids. A better temporal resolution of the data and available ion plasma moments would be helpful for further investigations. With ion plasma moments the spatial sizes of the analyzed PMs can be estimated. The size of the PM could give indications how much time the particle spends inside the PM and the gain of energy of the particle before it escapes the system.

Data Availability Statement

Juno MAG data used in this study were the 1-s PC files from data set "JNO-J-3-FGM-CAL-V1.0." Juno JEDI data were from the data set "JNO-J-JED-3-CDR-V1.0." The data sets can be found on the Planetary Data System at https://pds-ppi.igpp.ucla.edu/. The data analysis was done with Python using SciPy and seaborne packages among others.

Acknowledgments
A.B., E.A.K., E.E.G., and L.K. are supported by the Volkswagen Foundation Grant No. Az 97 742. E.A.K. is supported by the DFG project KR 4375/2-1 within SPP "Dynamic Earth." M.F.V. is supported by NASA Grant 80NSSC19K1263. Open access funding enabled and organized by Projekt DEAL.

References

Allen, R. C., Paranicas, C. P., Bagenal, F., Vines, S. K., Hamilton, D. C., Allegrini, F., et al. (2019). Energetic oxygen and sulfur charge states in the outer Jovian magnetosphere: Insights from the Cassini Jupiter flyby. *Geophysical Research Letters*, *46*(21), 11709–11717. https://doi.org/10.1029/2019GL085185

Angelopoulos, V., McFadden, J. P., Larson, D., Carlson, C. W., Mende, S. B., Frey, H., et al. (2008). Tail reconnection triggering substorm onset. *Science*, *321*(5891), 931–935. https://doi.org/10.1126/science.1160495

Artemyev, A. V., Clark, G., Mauk, B., Vogt, M. F., & Zhang, X. J. (2020). Juno observations of heavy ion energization during transient dipolarizations in Jupiter magnetotail. *Journal of Geophysical Research: Space Physics*, *125*(5), e27933. https://doi.org/10.1029/2020JA027933

Clark, G., Mauk, B. H., Kollmann, P., Paranicas, C., Bagenal, F., Allen, R. C., et al. (2020). Heavy ion charge states in Jupiter's polar magnetosphere inferred from auroral megavolt electric potentials. *Journal of Geophysical Research: Space Physics*, *125*(9), e2020JA028052. https://doi.org/10.1029/2020JA028052

Cleveland, W. S., & Devlin, S. J. (1988). Locally weighted regression: An approach to regression analysis by local fitting. *Journal of the American Statistical Association*, *83*(403), 596–610. https://doi.org/10.1080/01621459.1988.10478639

Cohen, C. M. S., Stone, E. C., & Selesnick, R. S. (2001). Energetic ion observations in the middle Jovian magnetosphere. *Journal of Geophysical Research*, *106*(A12), 29871–29881. https://doi.org/10.1029/2001JA000008

Connerney, J. E. P., Benn, M., Bjarno, J. B., Denver, T., Espley, J., Jorgensen, J. L., et al. (2017). The Juno magnetic field investigation. *Space Science Reviews*, *213*(1–4), 39–138. https://doi.org/10.1007/s11214-017-0334-z

DiBraccio, G. A., & Gershman, D. J. (2019). Voyager 2 constraints on plasmoid-based transport at Uranus. *Geophysical Research Letters*, *46*(19), 10710–10718. https://doi.org/10.1029/2019GL083909

Eastwood, J. P., Videira, J. J. H., Brain, D. A., & Halekas, J. S. (2012). A chain of magnetic flux ropes in the magnetotail of mars. *Geophysical Research Letters*, *39*(3). https://doi.org/10.1029/2011GL050444

Efron, B., & Tibshirani, R. (1994). *An introduction to the bootstrap*. Taylor & Francis.

Grigorenko, E. E., Malykhin, A. Y., Kronberg, E. A., Malova, K. V., & Daly, P. W. (2015). Acceleration of ions to suprathermal energies by turbulence in the plasmoid-like magnetic structures. *Journal of Geophysical Research: Space Physics*, *120*(8), 6541–6558. https://doi.org/10.1002/2015JA021314

Haggerty, D. K., Hill, M. E., McNutt, R. L., Jr., & Paranicas, C. (2009). Composition of energetic particles in the Jovian magnetotail. *Journal of Geophysical Research*, *114*(A2). https://doi.org/10.1029/2008JA013659

Jackman, C. M., Slavin, J. A., Kivelson, M. G., Southwood, D. J., Achilleos, N., Thomsen, M. F., et al. (2014). Saturn's dynamic magnetotail: A comprehensive magnetic field and plasma survey of plasmoids and traveling compression regions and their role in global magnetospheric dynamics. *Journal of Geophysical Research: Space Physics*, *119*(7), 5465–5494. https://doi.org/10.1002/2013JA019388

Kasahara, S., Kronberg, E. A., Krupp, N., Kimura, T., Tao, C., Badman, S. V., et al. (2011). Magnetic reconnection in the Jovian tail: X-Line evolution and consequent plasma sheet structures. *Journal of Geophysical Research*, *116*(A11). https://doi.org/10.1029/2011JA016892

Khurana, K., Kivelson, M., Vasyliunas, V., Krupp, N., Woch, J., Lagg, A., et al. (2004). Jupiter. The planet, satellites and magnetosphere. In *The configuration of Jupiter's magnetosphere* (pp. 593–616). Cambridge University Press.

Khurana, K. K., & Schwarzl, H. K. (2005). Global structure of Jupiter's magnetospheric current sheet. *Journal of Geophysical Research*, *110*(A7), A07227. https://doi.org/10.1029/2004JA010757

Kim, T. K., Ebert, R. W., Valek, P. W., Allegrini, F., McComas, D. J., Bagenal, F., et al. (2020). Method to derive ion properties from Juno jade including abundance estimates for O^+ and S^{2+}. *Journal of Geophysical Research: Space Physics*, *125*(2), e2018JA026169. https://doi.org/10.1029/2018JA026169

Kronberg, E. A., & Daly, P. W. (2013). Spectral analysis for wide energy channels. *Geoscientific Instrumentation, Methods and Data Systems*, *2*(2), 257–261. https://doi.org/10.5194/gi-2-257-2013

Kronberg, E. A., Grigorenko, E. E., Malykhin, A., Kozak, L., Petrenko, B., Vogt, M. F., et al. (2019). Acceleration of ions in Jovian plasmoids: Does turbulence play a role? *Journal of Geophysical Research: Space Physics*, *124*(7), 5056–5069. https://doi.org/10.1029/2019JA026553

Kronberg, E. A., Kasahara, S., Krupp, N., & Woch, J. (2012). Field-aligned beams and reconnection in the Jovian magnetotail. *Icarus*, *217*(1), 55–65. https://doi.org/10.1016/j.icarus.2011.10.011

Kronberg, E. A., Woch, J., Krupp, N., & Lagg, A. (2008). Mass release process in the Jovian magnetosphere: Statistics on particle burst parameters. *Journal of Geophysical Research*, *113*(A10), A10202. https://doi.org/10.1029/2008JA013332

Kronberg, E. A., Woch, J., Krupp, N., Lagg, A., Daly, P. W., & Korth, A. (2008). Comparison of periodic substorms at Jupiter and Earth. *Journal of Geophysical Research*, *113*(A4). https://doi.org/10.1029/2007JA012880

Kronberg, E. A., Woch, J., Krupp, N., Lagg, A., Khurana, K. K., & Glassmeier, K.-H. (2005). Mass release at Jupiter: Substorm-like processes in the Jovian magnetotail. *Journal of Geophysical Research*, *110*(A3), A03211. https://doi.org/10.1029/2004JA010777

Mauk, B. H., Haggerty, D. K., Jaskulek, S. E., Schlemm, C. E., Brown, L. E., Cooper, S. A., et al. (2017). The Jupiter energetic particle detector instrument (JEDI) investigation for the Juno mission. *Space Science Reviews*, *213*(1–4), 289–346. https://doi.org/10.1007/s11214-013-0025-3

Radioti, A., Woch, J., Kronberg, E. A., Krupp, N., Lagg, A., Glassmeier, K.-H., & Dougherty, M. K. (2007). Energetic ion composition during reconfiguration events in the Jovian magnetotail. *Journal of Geophysical Research*, *112*(A6). https://doi.org/10.1029/2006JA012047

Slavin, J. A., Anderson, B. J., Baker, D. N., Benna, M., Boardsen, S. A., Gold, R. E., et al. (2012). Messenger and mariner 10 flyby observations of magnetotail structure and dynamics at mercury. *Journal of Geophysical Research*, *117*(A1). https://doi.org/10.1029/2011JA016900

Slavin, J. A., Baker, D. N., Craven, J. D., Elphic, R. C., Fairfield, D. H., Frank, L. A., et al. (1989). CDAW 8 observations of plasmoid signatures in the geomagnetic tail: An assessment. *Journal of Geophysical Research*, *94*(A11), 15153–15175. https://doi.org/10.1029/JA094iA11p15153

Slavin, J. A., Lepping, R. P., Gjerloev, J., Fairfield, D. H., Hesse, M., Owen, C. J., & Mukai, T. (2003). Geotail observations of magnetic flux ropes in the plasma sheet. *Journal of Geophysical Research*, *108*(A1), 1015. https://doi.org/10.1029/2002JA009557

Thomas, N., Bagenal, F., Hill, T., Wilson, J., Dowling, T., & McKinnon, W. (2004). *Jupiter: The planet, satellites and magnetosphere*. Cambridge University Press.

Torrence, C., & Compo, G. P. (1998). A practical guide to wavelet analysis. *Bulletin of the American Meteorological Society*, *79*(1), 61–78. https://doi.org/10.1175/1520-0477(1998)079<0061:APGTWA>2.0.CO;2

Vasyliunas, V. M. (1983). Plasma distribution and flow. In A. J. Dessler (Ed.), *Physics of the Jovian magnetosphere* (pp. 395–453). Cambridge University Press. https://doi.org/10.1017/CBO9780511564574.013

Vogt, M. F., Connerney, J. E., DiBraccio, G. A., Wilson, R. J., Thomsen, M. F., Ebert, R. W., et al. (2020). Magnetotail reconnection at Jupiter: A survey of Juno magnetic field observations. *Journal of Geophysical Research: Space Physics*, *125*(3), e2019JA027486. https://doi.org/10.1029/2019JA027486

Vogt, M. F., Jackman, C. M., Slavin, J. A., Bunce, E. J., Cowley, S. W. H., Kivelson, M. G., & Khurana, K. K. (2014). Structure and statistical properties of plasmoids in Jupiter's magnetotail. *Journal of Geophysical Research: Space Physics*, *119*(2), 821–843. https://doi.org/10.1002/2013JA019393

Vogt, M. F., Kivelson, M. G., Khurana, K. K., Joy, S. P., & Walker, R. J. (2010). Reconnection and flows in the Jovian magnetotail as inferred from magnetometer observations. *Journal of Geophysical Research*, *115*(A6). https://doi.org/10.1029/2009JA015098

Woch, J., Krupp, N., Khurana, K. K., Kivelson, M. G., Roux, A., Perraut, S., et al. (1999). Plasma sheet dynamics in the Jovian magnetotail: Signatures for substorm-like processes. *Geophysical Research Letters*, *26*(14), 2137–2140. https://doi.org/10.1029/1999GL900493